

Urban Heat Island associated with Land Use/Land Cover and climate variations in Melbourne, Australia



Nurul Syahira Mohammad Harmay^a, Daeun Kim^b, Minha Choi^{c,*}

^a Civil, Architectural, and Environmental System Engineering, Sungkyunkwan University, Suwon, 16419, Republic of Korea

^b Han River Basin Support Group, Presidential Water Commission, Hanam 12902, Republic of Korea

^c Department of Water Resources, Graduate School of Water Resources, Sungkyunkwan University, Suwon, 16419, Republic of Korea

ARTICLE INFO

Keywords:

Urban Heat Island
Community Land Model
Climate change
Land Use/Land Cover
Australia

ABSTRACT

Urbanization is known as one of the most prominent global problems that alter the atmosphere and land surface properties. The intensity of Urban Heat Island (UHI) associated with surface temperature and component attributes were assessed using the Community Land Model (CLM). The variations of UHI with Land Use/Land Cover (LULC) and climate variations were also investigated to provide a link among urbanization, surface energy balance interactions, and extreme hydroclimatic events which are drought ('big dry' and 'angry summer') and heavy rainfall ('big wet') in Melbourne, Australia. Generally, UHI demonstrated a uniform increasing trend with an $\sim 1.20 \pm 0.20^\circ\text{C}$ increment, along with urbanization expansion of +14.93 % from 2001 to 2014. Furthermore, urban area showed positive contribution to UHI based on Land Contribution Index (LCI). High surface temperatures also resulted in higher sensible heat flux (Q_h) and lower latent heat flux (Qle). During the multiple extreme climate events, the UHI biophysical drivers were majorly related to the convection reduction during 'big dry' (2001–2009), surface evaporative cooling during 'big wet' (2010–2011), and heat storage release during 'angry summer' (2012–2013). Overall, this analysis demonstrated correlation of UHI intensity and its component attributes with urban expansion, which was associated with LULC and climate variations in Melbourne.

1. Introduction

Urbanization is recognized as a primary interface between human activities and impacts on the climate (Jackson et al., 2010). Land Use/Land Cover (LULC) changes in urban areas have consequently altered natural surface conditions and modified the energy and hydrological balance of the overlying atmosphere (Chen et al., 2015; Morris & Simmonds, 2001). Urban surfaces possess higher surface temperatures and rougher structures than their surrounding rural areas, which have higher vegetation cover (Daramola & Balogun, 2019; Stewart & Oke, 2009). Furthermore, surface warming can alter the variation in albedo, thermal aerodynamic properties, hydrology, and morphology of the surface (Torok et al., 2001).

In addition to urban expansion, climate change also needs to be considered as an important element for sustainable water management and planning as it has potential impacts on local and regional scales (Amin et al., 2019). Salimi and Al-Ghamdi (2020) found that the key factors of climate change in urban areas are vulnerable towards the

built-environment and water resources management. Additionally, significant variations in air temperature and precipitation from climate change have occurred due to anthropogenic and natural disruption (Chung et al., 2004). Meanwhile, changes in LULC also affect the climate and modify physical properties of the land surface through biophysical effects and surface energy budgets (Betts et al., 2007). Hence, a comprehensive framework to provide links between atmosphere and land surface interactions on Earth is important.

A well-recognized urban climate phenomenon is known as Urban Heat Island (UHI), which can be described as the differences of surrounding temperature in dense urban zones and rural areas (Adams & Smith, 2014; Phelan et al., 2015). Surface observations, satellite data, and numerical simulations have been used widely to quantify the magnitude of UHI (Rizwan et al., 2008; Zhou et al., 2014). Son et al. (2017) investigated the impacts of the rapid urbanization on the spatial pattern and UHI intensity using Landsat imagery. They found that the Landsat data indicates the increasing of land surface temperature (LST) and contributed to the UHI formation, along with the urban

* Corresponding author at: Department of Water Resources, Graduate School of Water Resources, Sungkyunkwan University, 2066 Seobu-ro, Jangan-gu, Suwon, Gyeonggi-do, 16419, Republic of Korea.

E-mail addresses: nurulharmay@g.skku.edu (N.S. Mohammad Harmay), daeunkim@korea.kr (D. Kim), mhchoi@skku.edu (M. Choi).

development. Urban areas that have higher thermal conductivity due to construction and building materials have increased absorption of solar radiation and modified surface energy balance fluxes (Imran et al., 2019; Oke, 1988). Throughout the years, the UHI effect has worsened along with urbanization and industrialization processes (Zhang et al., 2010). Hence, the consequential impacts caused by UHI need to be carefully addressed since it is one of the most important environmental components (Gao et al., 2018).

The initialization of weather and regional climate model to estimate the land surface parameters can be primarily presented using land surface models (LSMs) forced with in-situ and satellite-based data (Serpelzoglou et al., 2010). The Community Land Model (CLM) is one of the LSM components for the Community Earth System Model (CESM) that examines the biological, physical, and chemical processes of ecological climatology. Additionally, the urban land unit in CLM is represented by five columns comprised of roof, pervious and impervious canyon floor, and sunlit and shaded walls (Oleson & Bonan, 2010). The extension and availability of parameters in CLM have permitted evaluation of climatic variations and the physical driving factors correlated with UHI and convection variations.

Numerous studies have investigated UHI mechanisms and have primarily focused on UHI intensity with temporal or spatial variations and environmental composition (Hart & Sailor, 2009; Li et al., 2011; Peng et al., 2012; Schwarz et al., 2011; Zhou et al., 2017). However, most of the studies did not address the link between UHI with LULC and climate variations in the cities. Coutts et al. (2007a, 2007b) elaborated on the impacts of urban density on the surface energy balance partitioning in Melbourne using CLM, but their study did not discuss the biophysical factor of UHI in the city. Zhao et al. (2014) revealed a positive correlation between daytime UHI and annual mean precipitation; however, they did not study the correlation between the impacts of UHI and other climatic parameters. Meanwhile, Singh et al. (2017) estimated the LST for UHI analysis by using the multiple remote sensing-based products and in-situ observations. They found that the LST was primarily affected by LULC and anthropogenic heat, but the effects of UHI towards other energy heat fluxes are excluded. Most recently, Fitria et al. (2019) analyzed the biophysical mechanism of UHI by linking El Niño-Southern Oscillation (ENSO) events and UHI driving factors. While this finding was based on the derived energy balance, inter-comparison of LULC within urban land and climate change has not been fully studied. In short, a fundamental knowledge gap exists for understanding the response of local climate change and surface energy balance toward dynamic land-use and UHI.

The main objectives of this study were to (1) quantify UHI intensity and its attributes using the model simulation approach, (2) analyze hydro-meteorological alterations caused by urbanization and local climate sensitivity, and (3) evaluate the relationship between UHI with LULC and climate variations. This paper describes the UHI impact assessment which involves different scenarios of LULC and climate variations to recognize key influencing factors of land use changes and climate uncertainty toward urbanization effects. We incorporated the model simulation approach from CLM, MODIS satellite products, and climate observations and indices analysis to achieve the objectives of this study. The partitioning of the major contributor of the UHI components that correlates with LULC and climate parameters is also being investigated. Overall, we provided a systematic framework that integrated the model simulation, satellite observations, and climate indices to improve hydrological interactions and climate variations in the land surface atmosphere. This study also enhances the understanding of the impact of land changes and climate footprints toward UHI that affect the urban environment and community.

2. Materials and methods

2.1. Study area

The city of Melbourne, the capital of Victoria, Australia, was chosen as a study area (Fig. 1). Melbourne has different land cover types of farmland, conservation, natural environments, residential, industrial areas, and rivers and associated creeks (Jamei et al., 2019). Melbourne is recognized as the second most populous city in Australia with a population of 4.9 million, along with a rapid urbanization rate and increasing population density (Imran et al., 2019). The Köppen-Geiger climate classification in Melbourne is classified as 'Cfb,' which can be described as warm temperate, fully humid, and warm summer. The annual average precipitation for Melbourne is around 531 mm with an average maximum temperature during mild winter (July) of 13.4 °C and an average January (moderate hot summer) maximum temperature of 25.8 °C (Keay & Simmonds, 2005).

Since the beginning of the 21st century, Australia has experienced a series of extreme climatic changes. It began with a prolonged drought that occurred in 2001 and lasted until the end of 2009 (Van Dijk et al., 2013). This event which is also known as a 'big dry' (or 'Millennium Drought') was determined based on the longest period with the rainfall occurrences below the median observations since 1900, according to Bureau of Meteorology Australia. The prolonged drought period was ended with heavy rainfall event and flooding from 2010 to 2011, which is also known as a 'big wet' (Heberger, 2019). In summer 2012, an extensive high temperature period called 'angry summer' was occurred in the late December 2012 until the mid of January 2013 (Bureau of Meteorology, 2013). These climatic extremes had a negative impact on ecosystem productivity and water resources over the Australian region (Sewell et al., 2016; Van Dijk et al., 2013).

2.2. Dataset

2.2.1. Hydro-meteorological observation data

The observational, hydro-meteorological parameters were obtained from two eddy covariance flux towers and one climate station in the Victoria region (Fig. 1a, Table 1). One eddy covariance tower (urban site) and selected climate station were located in the city of Melbourne, while another rural site was located within an 80 km radius from the urban and climate sites. The FLUXNET global network linked multiple flux measurements across America, Europe, Asia, Africa, and Australia. The AU-Wom Wombat (rural) site is one of the available flux tower sites in Melbourne, Australia, obtained from Fluxnet2015 (Pastorello et al., 2020). This site is dominated by woody vegetation (>60 %) with evergreen broadleaf forests (EBF) and IGBP characteristics. It is located at an elevation of 705 m with a 5-year period of available data (2010–2014) measured by the University of Melbourne research team. The time period considered in this study was 2001–2014, which included the interval time for flux tower model validation from this flux tower site.

The second eddy covariance flux tower is the urban flux tower site Au-Preston (urban), located in the northern part of the city of Melbourne in Preston, with moderately developed low-density housing. The instrument was installed at a height of 40 m (z_m) on a pre-existing tall telecommunications tower in Melbourne. The radial basis function (RBF) approach was used to fill the missing data from nearby stations or the Monash University weather station (Coutts et al., 2007b). Shortwave and longwave radiation, net radiation (R_n), sensible heat flux (Q_h), latent heat flux (Q_{le}), temperature, relative humidity, and precipitation were recorded at this site for each half-hourly period from August 2003 until November 2004 (Coutts et al., 2007a, 2007b).

Long-term annual precipitation and temperature were obtained from the nearest meteorological station for climate variation analysis. Site 86282 (Melbourne Airport) climate station was chosen due to the availability of long-term climate data in Melbourne (<http://bom.gov.au>). This station employed a Global Positioning System (GPS) for

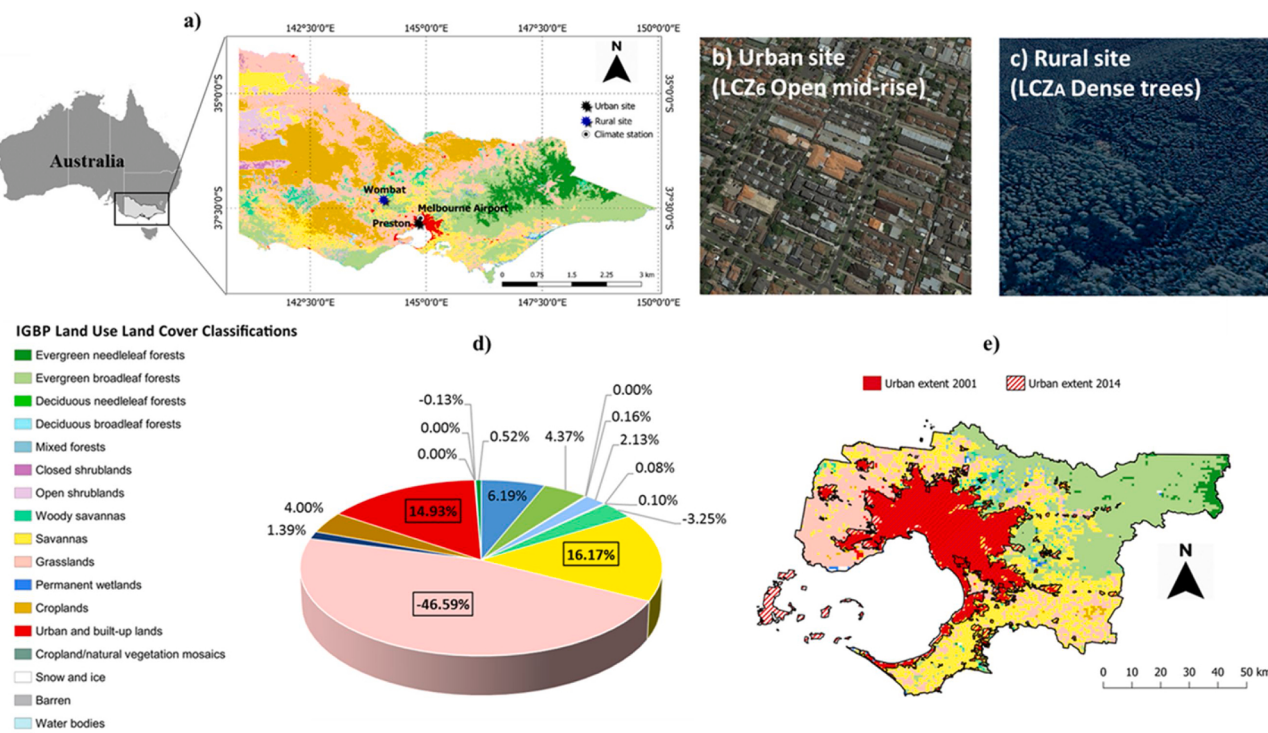


Fig. 1. a) Locations of selected sites with aerial photographs around b) urban site and c) rural site, d) percentage change of LULC between 2001 and 2014, and e) LULC map of Melbourne based on IGBP classifications, respectively.

Table 1

Characteristics of the study sites at Preston, Wombat, and Melbourne Airport.

Site name	Site ID	Site type	IGBP Classifications	Latitude	Longitude	Elevation	Data availability
Preston	Mb03m	Urban flux tower	Urban and built-up lands	37.72 °S	145.00 °E	40.0 m	2003–2004
Wombat	AU-Wom	FLUXNET site	EBF (evergreen broadleaf forests)	37.42 °S	144.09 °E	705.0 m	2010–2014
Melbourne Airport	Site 86282	Climate station	Urban and built-up lands	37.67 °S	144.83 °E	113.4 m	1970–2020

geographic positioning. The tower is located at an elevation of 113.4 m with a 118.8 m barometer height. In this study, data for mean annual precipitation (P_{mean}), mean annual temperature (T_{mean}), maximum annual temperature (T_{max}), and minimum annual temperature (T_{min}) were generated from 2001 to 2014.

2.2.2. Satellite data

Remote sensing data from the Moderate Resolution Imaging Spectroradiometer (MODIS) were used to determine the LULC classification and their respective land surface temperature. MODIS land cover data (MCD12Q1) were used to construct an LULC map of the city of Melbourne to investigate the changes in the urban-rural areas of the city. Land classification data were established based on the International Geosphere–Biosphere Programme (IGBP) land classification system. We also used the MODIS Aqua LST 1 km spatial resolution product (MYD11A2) to estimate the surface temperature that corresponded to each dominant LULC types in the study area.

2.2.3. Global Land Data Assimilation System (GLDAS)

The Global Land Data Assimilation System (GLDAS) is a global dataset that combines satellite and ground-based observations by integrating data assimilation and advanced LSM. Currently, various LSMs are run by GLDAS, namely NOAH, Mosaics, Variable Infiltration Capacity (VIC), and CLM (Rodell et al., 2004). GLDAS provides various temporal and spatial ground-based products of the global fluxes. More details and information about the GLDAS documentation are available at NASA's Hydrology Data and Information Services Center's website (<http://disc.sci.gsfc.nasa.gov/hydrology>).

2.2.4. Climate index

The southeastern part of Australia has suffered continuous climate variability including a decline in rainfall and an increase in background temperature due to its highly concentrated population and agricultural production (Murphy & Timbal, 2008). In this study, we used the Southern Annular Mode (SAM), the El Niño-Southern Oscillation (ENSO), and the Indian Ocean Dipole (IOD) climate modes to represent climate dynamics along with extreme hydroclimatic events namely 'big dry', 'big wet', and 'angry summer' in the study area. The time-series data of the climate index namely Southern Annular Mode Index (SAMI), Southern Oscillation Index (SOI), and Dipole Mode Index (DMI) were obtained from the National Oceanic and Atmospheric Administration (NOAA) to indicate the SAM, ENSO, and IOD dynamics, respectively. The data were acquired as a monthly time-series covering the period from 2001 to 2014 (Fig. 2a).

The SAM plays a significant role in climate variations in the circulation of the Southern Hemisphere over a broad temporal scales (Marshall et al., 2018). SAM was utilized to identify and measure the SAM changes between the middle and high latitudes of the Southern Hemisphere. According to Bureau of Meteorology Australia, positive SAM results in higher pressure and dry conditions in southern Australia, while the negative phase indicates more storms and rainfall. SAM is also known as a major climate mode in the southern hemisphere circulation, and it has been shown to have a correlation with Australian rainfall.

ENSO which encompassing "El Niño", "La Niña", and "Neutral" causes a periodic variation in sea surface temperature (SST) and atmospheric pressure over the tropical eastern of the Pacific Ocean. The El Niño phase corresponds to the ocean warming (warming phase) while

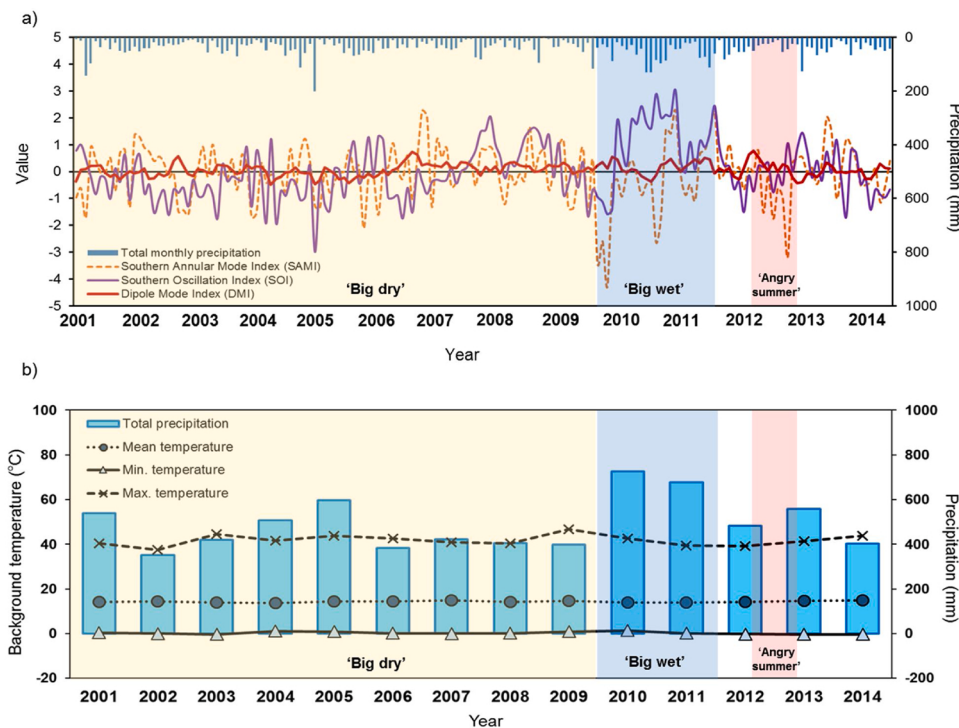


Fig. 2. Temporal variations of a) total monthly precipitation with Southern Annular Mode Index (SAMI), Southern Oscillation Index (SOI), and Dipole Mode Index (DMI) and b) total annual precipitation with maximum, minimum, and mean temperatures from 2001 to 2014 over Melbourne. The shaded areas indicate hydro-climatic events of 'big dry' (yellow), 'big wet' (blue) and 'angry summer' (red).

the La Niña involves the cooling of the tropical Pacific Ocean (cooling phase) (Trenberth, 1997). In this study, the ENSO dynamics of the Pacific Ocean were measured based on the SOI (Kawamura et al., 1998; Yan et al., 2011), which can be defined as the difference between the sea level pressure at Tahiti in the eastern Pacific, and Darwin in the western Pacific Ocean (Trenberth, 1984). We used the standardized measures by Bureau of Meteorology Australia to indicate the ENSO events in the study area: negative values of the SOI below -7 for El Niño and positive values higher than +7 for La Niña.

DMI is an index used for IOD that presents the SST gradient between the southeastern and western equatorial of the Indian Ocean (Rayner et al., 2003). According to Saji et al. (1999), the DMI is independent with the ENSO occurrences, where the positive DMI is often related to El Niño while the La Niña are associated with negative DMI. The positive IOD phase indicates lower precipitation over the eastern basin and warmer surface waters in the western basin. Contrastingly, the eastern basin experienced higher rainfall and colder surface waters in the western basin during the negative IOD phase (Menezes & Vianna, 2019).

Fig. 2a shows that the high polarity index of the SAM was significantly correlated with the decrease in rainfall during the 'big dry' event between 2001–2009 due to the positive SAMI that exhibited warmer and drier temperature counterparts (van Lipzig et al., 2008). Besides, during the 'big dry' period, the SOI showed an inconsistent trend with the lowest (negative value) in the year 2005 which indicates the warmest and driest phase in Melbourne, consistent with Taschetto et al. (2016). In contrast, the uniform positive SOI between 2010–2011 exhibited higher total annual precipitation during the 'big wet' event (Fig. 2b), similar with previous study of the rainfall variability over the southeast Australia (King et al., 2013). Therefore, this confirms the findings by Ummenhofer et al. (2011) which showed that the La Niña effect is more prominent in the southern part of Australia, particularly during the interannual scales and prolonged wet periods. On the other hand, the IOD that is indicated by DMI showed more positive phase during the drought event from 2001 to 2009, consistent with Ummenhofer et al. (2009) which proved that the 'big dry' is majorly driven by IOD.

2.3. Model descriptions

The CLM is a land component of the Community Earth System Model (CESM) that was developed at the National Center of Atmospheric Research (NCAR) (Oleson et al., 2013). CLM has a higher capability for evaluating various temporal scale of climate variability based on soil the hydrological parameters, runoff-generation schemes, snow, and albedo-related parameters (Umair et al., 2019). The CLM consists of five land units of glacier, lakes, vegetation, wetland, and urban at the first level. The CLM simulation could be run coupled to an atmospheric model or with 'offline' forcing with the data atmosphere model (Kiehl & Gent, 2004).

We used CLM version 4 to produce hydro-meteorological parameters and surface energy fluxes. CLM version 4 is highly compatible with investigations into the role of land processes in climate change, land cover and land use change, and urbanization as well as mechanistic feedback studies between terrestrial and broader earth systems (Lawrence et al., 2011). The input atmospheric data of longwave radiation, shortwave radiation, precipitation, pressure, specific humidity, relative humidity, air temperature, and wind speed were carefully prepared for the 'offline' mode (uncoupled from an active atmospheric model) of the model. In this study, we used eddy-covariance data (CLM-OBS) and the GLDAS dataset (CLM-GLDAS) for input forcing at both sites.

2.4. Model performance

Pearson's correlation coefficient (R), root-mean square error (RMSE), bias, and index of agreement (IOA) were used to evaluate model performance. The details of these evaluation metrics are as follows:

$$RMSE = \sqrt{\sum_{i=1}^n \frac{(C_i - O_i)^2}{n}}, \quad (1)$$

$$Bias = \sum_{i=1}^n (C_i - O_i) / n, \quad (2)$$

and

$$IOA = 1 - \frac{\sum_{i=1}^n (C_i - O_i)^2}{\sum_{i=1}^n (|C_i - \bar{O}| + |O_i - \bar{O}|)^2}, \quad (3)$$

where C_i and O_i represent model-based (CLM) and observed values, respectively, while the mean of the observed data is denoted by \bar{O} .

2.5. Land Contribution Index (LCI)

Land Contribution Index (LCI) is a quantitative indicator introduced by Huang et al. (2019) to further quantify the relationship between land use types and UHI. In this study, the sample points for each dominant land use types were examined to derive the land surface temperature for the particular land use types. The LCI can be approximated as follows:

$$LCI_i = (T_i - M) \times P_i \quad (4)$$

From Eq. (4), T_i is the average temperature of the i -th land use types, M is the average temperature of the study area, i refers to the number of land use types, P_i represents the proportion of the i -th land use type to the entire area. The LCI can be categorized into two indicators where, the $LCI \geq 0$ denotes that the respective land use type has a positive effect on UHI and $LCI < 0$ indicates that the land use type is not severe to the UHI effect.

2.6. Urban characteristics

In general, UHI is defined as the differences in urban and rural temperatures. It can also be further categorized into two broad types, where it can be assessed by either in-situ temperature from urban and rural weather stations (Zhou et al., 2016) or land surface temperature (LST) from satellite-based observations (Hart & Sailor, 2009; Wu et al., 2014). In this study, the temperature differences between urban and rural sites from the CLM simulation were initially calculated to explain the UHI trends. These sites were selected based on Local Climate Zones (LCZ) classification by Stewart and Oke (2012) which corresponds to LCZ_A (dense trees) for rural site and LCZ₆ (open low-rise) for the urban site. Next, the UHI calculations from analysis of the surface energy balance were evaluated, along with the attributes of its components.

We used model-predicted ΔT from surface energy balance analysis (Zhao et al., 2014) to quantify the UHI attributes in Melbourne, Australia. The equation was derived from a study by Lee et al. (2011), but there were some limitations of the biophysical driving factors in the original equation. They assumed that incoming solar radiation, incoming longwave radiation, and air temperature of the adjacent land types were the same. In addition, they only revealed the radiative forcing term from albedo changes and energy redistribution, while neglecting the minor terms, such as surface emissivity changes. The improvement in UHI intensity (ΔT) based on total UHI contributions could be approximated as follows:

$$\Delta T = \frac{\lambda_0}{1+f} \Delta R_n^* + \frac{-\lambda_0}{(1+f)^2} (R_n^* - Q_s + Q_{AH}) \Delta f_1 + \frac{-\lambda_0}{(1+f)^2} (R_n^* - Q_s + Q_{AH}) \Delta f_2 + \frac{-\lambda_0}{1+f} \Delta Q_s + \frac{\lambda_0}{1+f} \Delta Q_{AH} \quad (5)$$

with

$$f = \frac{\lambda_0 \rho C_p}{r_a} \left(1 + \frac{1}{\beta} \right) \quad (6)$$

$$R_n^* = (1 - a) K_\downarrow + L_\downarrow - (1 - \varepsilon) L_\downarrow - \varepsilon \sigma T_a^4 \quad (7)$$

$$\Delta f_1 = \frac{-\lambda_0 \rho C_p}{r_a} \left(1 + \frac{1}{\beta} \right) \frac{\Delta r_a}{r_a} \quad (8)$$

$$\Delta f_2 = \frac{-\lambda_0 \rho C_p}{r_a} \frac{\Delta \beta}{\beta^2} \quad (9)$$

where T_s is surface temperature, $\lambda_0 = 1/4\varepsilon\sigma T_s^3$ is the local climate sensitivity, f is the energy redistribution factor, R_n^* is the apparent net radiation, ρ is the air density, C_p is the specific heat of air at a constant pressure, r_a is the aerodynamic resistance to heat diffusion calculated as $r_a = \frac{\rho C_p (T - T_a)}{Q_h}$, β is the Bowen-ratio calculated as $\beta = \frac{Q_h}{Q_e}$, a is the surface albedo, K_\downarrow is the incoming solar radiation, L_\downarrow is the incoming longwave radiation, ε is the surface emissivity, σ is a Stefan-Boltzmann constant, and T_a is the air temperature at a reference height.

In Eq. (5), the right-hand side represents radiation balance (Term 1), convection efficiency (Term 2), surface evaporative cooling (Term 3), heat storage (Term 4), and anthropogenic heat (Term 5). The UHI calculation was performed separately for 1:00 and 13:00 local times and all the parameters were derived from forcing data and model-prediction from the CLM.

3. Results and discussion

3.1. Model evaluations

First, to attain UHI intensity, the T_s from 2001 to 2014 for both urban and rural sites were obtained from CLM simulation. Therefore, to assure CLM capability in simulating the hydro-meteorological parameters in this study, their accuracies and performances were validated with observed data. For UHI analysis, T_s was used to verify the output results from CLM-OBS and CLM-GLDAS using the R, RMSE, Bias, and IOA methods (Table 3). Fig. 3 shows the scatterplots of the observed and simulated T_s for daytime and nighttime at the urban and rural sites.

The urban site showed the best agreement for daytime T_s with forcing from the flux tower, and R and IOA values of 0.92 and 0.99, respectively. In contrast, the CLM-OBS underestimated the nighttime T_s with a negative bias of -0.75°C at the urban site due to the limited urban sub-grid levels in the model (Cao et al., 2016; Fitria et al., 2019). In the rural site, the simulated T_s from flux tower forcing showed better correlation than that of the CLM-GLDAS, with an R value of 0.90 and IOA of 0.96 during the daytime. Nighttime T_s also demonstrated reliable results that showed R and IOA values of 0.76 and 0.92, respectively. The simulated T_s from CLM-OBS showed better agreement than that of the CLM-GLDAS at both urban and rural sites because of the advantages from highly accurate flux tower forcing (Dirmeyer et al., 2018).

Both sites demonstrated the best results for CLM-GLDAS during the daytime, with R and IOA values of 0.87 and 0.97 (rural) and of 0.85 and 0.98 (urban), respectively. CLM-GLDAS captured the observed data for nighttime T_s at the rural site with only slight overestimation, denoted by a bias of 1.70°C . GLDAS improved the simulation with a high degree of agreement with observed data during the daytime due to evaporation parameterization and anthropogenic heat draw-up of the impervious surface, a similar pattern to the results of a previous study of the Integrated Urban Land Model (IUM) and Common Land Model (CoLM) (Ogden et al., 2015).

In addition, we compared the simulated surface energy fluxes Q_h and Q_e with observed data using different atmospheric forcing (Table 4). This was performed because further analysis of LULC and UHI component attributes in this study depended on simulated Q_h and Q_e for convection efficiency (Term 2) and evaporative cooling (Term 3) of UHI attribute analysis. From the statistical results, CLM-OBS showed reliable improvement to simulate Q_h at the urban site, with R and IOA values of 0.85 and 0.90 during the daytime and of 0.75 and 0.86 during the

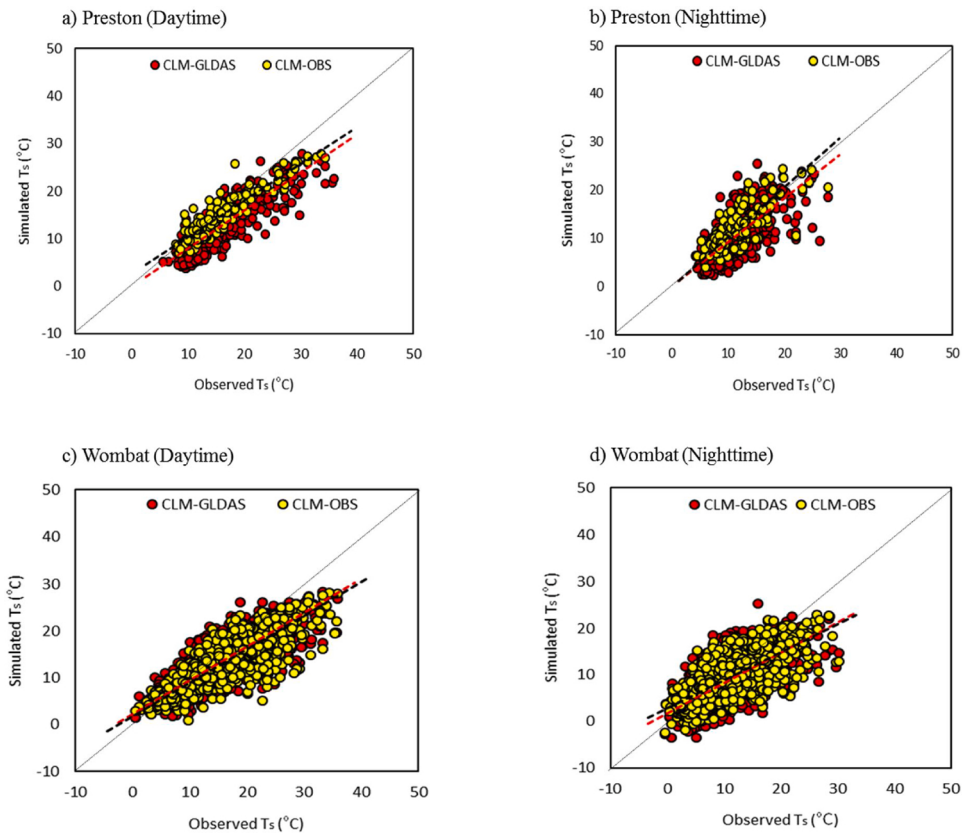


Fig. 3. Scatter plots of surface temperature (T_s) during the daytime and nighttime between observations from flux towers and the simulation using GLDAS (CLM-GLDAS) and flux tower forcing (CLM-OBS) at the Preston site (a, b) from August 2003 to November 2004 and at the Wombat site (c, d) from January 2010 to December 2014, respectively.

nighttime, respectively. CLM-GLDAS underestimated Q_h compared to CLM-OBS due to the surface temperature estimation in CLM associated with excess shortwave radiation (Kim et al., 2016; Winter & Eltahir, 2010).

In contrast, CLM-GLDAS indicated the best performance in simulating Q_{le} during the daytime, with only slight overestimation of 5.22 W

m^{-2} . During the day, Q_{le} was dominant, and it continued as a positive flux at night due to higher moisture availability in Melbourne (Coutts et al., 2007b). In general, all the output results from the simulation corresponded well with the observed data for both sites during the study period. Different forcing data used in CLM also showed high capability in simulating the output variables of T_s , Q_h , and Q_{le} .

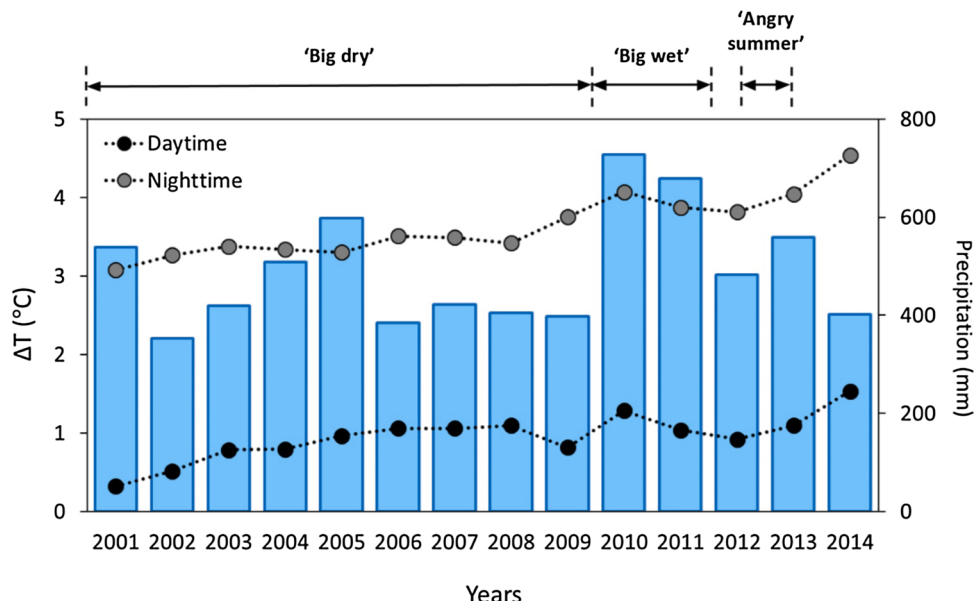


Fig. 4. Temporal variations in simulated UHI intensity (ΔT) for the daytime and nighttime with annual precipitation from 2001 to 2014 in Melbourne. ΔT is determined from surface temperature differences between the Preston urban site and Wombat rural site ($\Delta T = T_{s(\text{urban})} - T_{s(\text{rural})}$).

3.2. Trends in surface temperature difference (ΔT)

To assess the trends in UHI intensity in Melbourne, we followed the methodology employed in a previous study to explain the first definition of UHI that could be denoted as the temperature difference between urban and rural areas (Sun et al., 2019). We initially quantified the UHI intensity from simulated T_s to analyze the temporal variations in UHI from 2001 to 2014 for the daytime (13:00) and nighttime (01:00). UHI analysis based on temporal variations in simulated ΔT for 14 years showed increasing trends during the daytime and nighttime (Fig. 4).

The lowest ΔT was observed in the year 2001. Meanwhile, the highest ΔT value was seen in 2014 for both daytime and nighttime. In 2014, daytime ΔT increased by $\sim 1.40^\circ\text{C}$ compared to that in 2001, whereas the nighttime ΔT showed an increasing trend of $\sim 1.20^\circ\text{C}$. Melbourne experienced the LULC change with more urban expansion in 2014 than in 2001 (Fig. 1d, e), which contributed to the increasing trend in ΔT . Previous research conducted by National Aeronautics Space Administration (NASA) in 2006 found that higher temperatures from urban warming led to unstable air, resulting in rain-producing clouds and higher precipitation events. The highest annual precipitation was recorded in 2010 at an intensity of 727 mm and coincided well with relatively high daytime and nighttime ΔT . Brook (2015) also showed that, when surface temperature increased, a high evaporation rate occurred, which resulted in increased precipitation.

However, the highest ΔT recorded in 2014 did not show evidence of high rainfall occurrence for that particular year. This inconsistent relationship between ΔT and precipitation might have occurred due to the dynamic climate modes during that particular year, as shown in Fig. 2a. In 2014, the SOI exhibited relatively low negative value which resulted in warmer conditions and high temperature increase and warmer conditions in Melbourne. This result indicated that precipitation and urban warming are not fully dependent, consistent with Manoli et al. (2019). However, they were also correlated with climate shifts (Yang et al., 2019). In addition, the combined effects of urban growth and climate change led to a higher ΔT than when only one factor was considered (Chapman et al., 2017). Overall, the ΔT in Melbourne experienced an increasing trend from 2001 to 2014, which showed that surface temperature warming corresponded well with both urbanization and climate change effects.

3.2.1. Role of LULC in UHI intensity

Statistical results illustrated from the pie chart in Fig. 1d demonstrated that the dominant land use types were urban and built-up lands, grasslands, and savannas. These land use types were characterized by herbaceous species (grasslands), 10–30 % tree cover (savannas), and at least 30 % of impervious surface area including building, asphalt, and vehicles (urban and built-up lands). Our analysis also demonstrated that the urban and built-up areas were agglomerated in the coastal part of Melbourne, while grasslands and savannas were evenly distributed in the eastern, southern, and western plains of Melbourne. In 2014, these major land cover types experienced changes of +14.93, -46.59, and +16.17 % for urban and built-up, grasslands, and savannas, respectively (Fig. 1d). Generally, urban land class changed at relatively high rates with a positive indicator in 2014 compared to 2001. In addition, the reduction of grasslands also appeared to be the drivers of UHI effect in the study area.

In order to further evaluate the relationship between UHI and LULC in Melbourne, the contribution index of different LULC types to the UHI were quantified by using LCI. Fig. 5 demonstrated the contribution index of major LULC types in the study area namely savannas, grasslands, and urban and built-up area for the year 2001 and 2014. We only considered three LULC types for our LCI calculation based on the dominant land cover types from the analysis shown in Fig. 1d. Besides, we only compared the LULC changes for two years to provide distinct justification for the lowest and highest ΔT obtained in Section 3.2 (Fig. 4).

With the expansion of urbanization process that occurred in 14 years, 20.48 % of the constructed urban area in 2014 deployed to higher UHI contribution compared to 19.00 % in 2001 (Table 2). The positive contribution of urban and built-up area with UHI was also indicated with the increment of LCI value of 0.31 in 2014 compared to 0.26 in 2001 (Fig. 5). This trend showed that the urban expansion in the later year has contributed more to the UHI intensity in Melbourne. Contradictorily, savannas and grasslands showed a negative impact on the UHI for 2001 (2014) with LCI values of -0.27 (-0.33) and -0.43 (-0.28), respectively (Fig. 5). The results showed that a higher percentage of savannas in the later year have contributed to the more negative LCI value with more mitigation effect towards UHI, compared to grasslands area that experienced decrement of -46.59 %. This observation proved that urban green spaces had the alleviating function to reduce the thermal environment and UHI intensity, consistent with previous study (Huang et al., 2019). In 2001, the LCI of grasslands was lower than

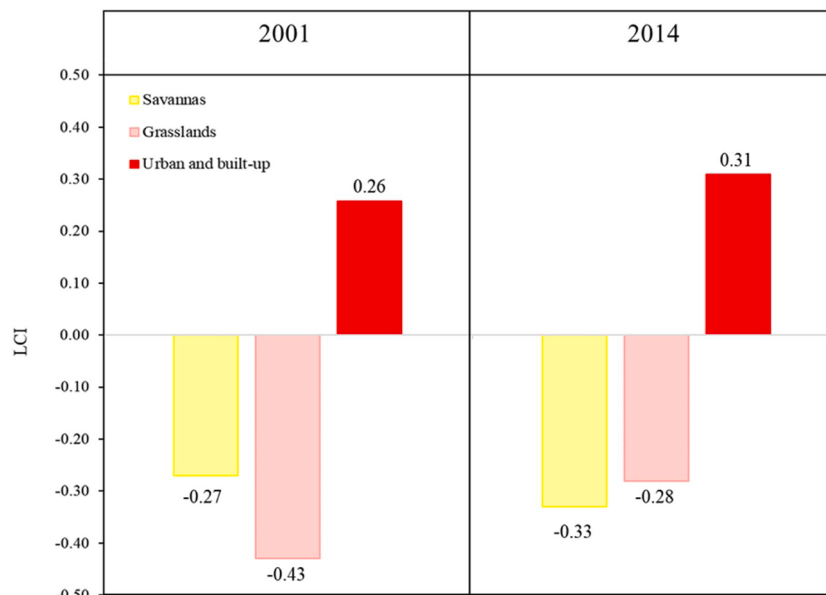


Fig. 5. Land Contribution Index (LCI) for dominant Land Use/Land Cover (LULC) classifications in the study area for the year 2001 and 2014.

Table 2

Spatial extents and proportions of Land Use/Land Cover (LULC) classifications in the study area.

Land Use/Land Cover classifications	Proportions			
	Area (pixel)	Percent (%)	Area (pixel)	Percent (%)
	2001	2001	2014	2014
ENF	176182919	2.00	230308470	2.61
EBF	2388383965	27.16	2430250075	27.59
DNF	–	–	–	–
DBF	–	–	1353244	0.02
Mixed forests	113070424	1.29	131748053	1.50
Closed shrublands	–	–	677547	0.01
Open shrublands	–	–	386331	0.01
Woody savannas	102917386	1.17	74785696	0.85
Savannas	2359055629	26.82	2503606751	28.42
Grasslands	1876293118	21.33	1473880224	16.73
Permanent wetlands	30625891	0.35	42787974	0.49
Croplands	52943528	0.60	87841268	1.00
Urban and built-up	1671455074	19.00	1804083813	20.48
Cropland/natural vegetation	–	–	–	–
Snow and ice	–	–	–	–
Barren	1651269	0.02	529736	0.01
Water bodies	22357192	0.25	26958860	0.31

savannas; however, in the later year, they had less difference in the heat contribution due to the decrement of grasslands area and the expansion of savannas in 2014. According to Salleh et al. (2015), grasslands provide vegetation coverage for the land, which can help to increase the surface cooling system for the city compared to that of urban land with lower surface albedo and high surface heat capacity.

As indicated above, urban expansion was highly contributed to the higher UHI effect in the study area for the year 2014. The difference in urban and built-up land in 2014 compared to 2001 significantly changed urban T_s as well as UHI intensity in the temporal scale by $\sim 1.40^\circ\text{C}$ during the daytime and $\sim 1.20^\circ\text{C}$ during the nighttime (Fig. 4). Besides, the conversion of natural vegetation to urban area caused numerous alterations towards the Earth's surface energy balance due to the urban surface characteristics of thermal, radiation, moisture, and aerodynamic properties (Silva et al., 2018). Fig. 6 illustrates the diurnal variations of simulated ΔT with Q_h and Q_{le} for the years 2001 and 2014, respectively. Due to the increase in urban area, UHI intensity showed the largest

differences from 00:00 to 07:00, when ΔT was heightened by $\sim 1.40 \pm 0.3^\circ\text{C}$. In contrast, the difference in UHI growth from 18:00 to 23:00 increased by approximately $\sim 1.10^\circ\text{C}$.

CLM simulated higher diurnal ΔT in 2014 compared to 2001, with higher Q_h and lower Q_{le} in 2014, which was consistent with a previous UHI intensification study (Li et al., 2015). The increment of Q_h and reduction of Q_{le} led to higher ΔT , which also resulted in more longwave radiation emitted from the land surface into the atmosphere (Coutts et al., 2007b). Vegetation cover that is significantly reduced due to urbanization will also increase the surface roughness and lead to higher Q_h and lower Q_{le} (Ma et al., 2014). In general, a high urbanization rate later in the year escalated the UHI intensity due to higher heat production from pavement, building materials, and transportation from the urban environment, which then altered Q_{le} , Q_h , heat storage (Q_s), and net radiation (R_n) (Oke, 1988). Overall, the urbanization caused by LULC resulted in higher ΔT , which consequently shifted the trends of Q_h and Q_{le} in Melbourne for the period of 2001 to 2014.

3.2.2. Relationship between UHI and climate change

To unfold the issues regarding UHI intensification with climate change impacts in the southern part of Australia, the relationships of ΔT with total precipitation and variation in temperature were addressed. Simulated daytime and nighttime ΔT were analyzed with P_{mean} , T_{mean} , T_{max} , and T_{min} from 2001 to 2014 (Fig. 7). A trend between ΔT and P_{mean} for the 14-year period is shown in Fig. 7a, with a positive relationship during the daytime ($R = 0.07$) but a negative relationship during the nighttime ($R = -0.10$). Precipitation can be partially described by soil moisture, where a higher heat capacity stored in soil moisture during the day was released during the nighttime (Oke et al., 1991; Zhou et al., 2016). Therefore, this finding suggests that ΔT highly affects P_{mean} , with warmer conditions during the daytime than the nighttime ΔT .

This result also demonstrated a positive correlation of UHI with T_{max} during the daytime and nighttime with R values of 0.27 and 0.23, respectively (Fig. 7c). This relationship indicated that T_{max} increased as ΔT increased. In contrast, ΔT showed a negative relationship with T_{min} over the 14-year period. The positive link between ΔT and T_{max} coincided with the high correlation of SAM with T_{max} , whereas SAM were weaker with their T_{min} counterparts (Hendon et al., 2007). Similarly, T_{max} also correlated with ENSO especially in the southern part of Australia, where the increase of T_{max} consequently decrease the T_{min} and precipitation under El Niño effects (Jakob & Walland, 2016).

Table 3

Statistical analysis of observed and simulated surface temperatures (T_s) from the flux tower, CLM using flux tower forcing (CLM-OBS), and GLDAS (CLM-GLDAS) at the Preston (urban) and Wombat (rural) sites with RMSE and bias in $^\circ\text{C}$ units.

Preston (urban)				Wombat (rural)				
Daytime		Nighttime		Daytime		Nighttime		
	CLM-OBS	CLM-GLDAS	CLM-OBS	CLM-GLDAS	CLM-OBS	CLM-GLDAS	CLM-OBS	CLM-GLDAS
R	0.92	0.85	0.78	0.67	0.90	0.87	0.76	0.71
RMSE	1.16	1.66	2.22	2.36	1.71	1.51	1.24	1.87
Bias	1.09	2.80	-0.75	0.27	2.24	1.74	1.21	1.70
IOA	0.99	0.98	0.99	0.99	0.96	0.97	0.92	0.99

Table 4

Statistical analysis of observed and simulated sensible heat fluxes (Q_h) and latent heat fluxes (Q_{le}) from the flux tower, CLM using flux tower forcing (CLM-OBS), and GLDAS (CLM-GLDAS) at the Preston (urban) site with RMSE and bias in units of W m^{-2} .

Q_h				Q_{le}				
Daytime		Nighttime		Daytime		Nighttime		
	CLM-OBS	CLM-GLDAS	CLM-OBS	CLM-GLDAS	CLM-OBS	CLM-GLDAS	CLM-OBS	CLM-GLDAS
R	0.85	0.71	0.75	0.69	0.76	0.83	0.68	0.65
RMSE	33.76	38.12	52.12	43.88	32.77	30.44	25.22	16.51
Bias	9.02	8.32	-7.54	-9.73	6.51	5.22	9.98	-9.28
IOA	0.90	0.35	0.86	0.67	0.55	0.68	0.72	0.75

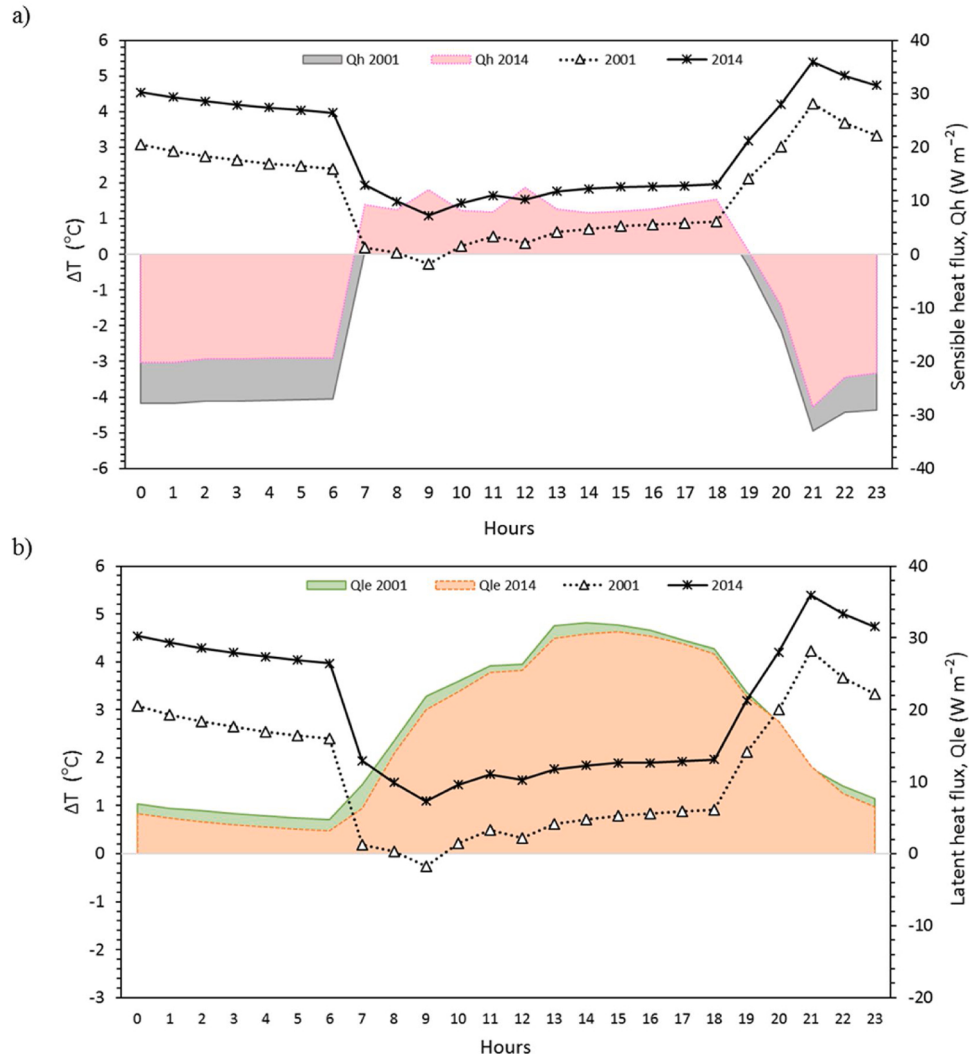


Fig. 6. Average diurnal variations of simulated ΔT with a) sensible heat flux (Q_h) and b) latent heat flux (Q_{le}) at the Preston (urban) site for the years of 2001 and 2014.

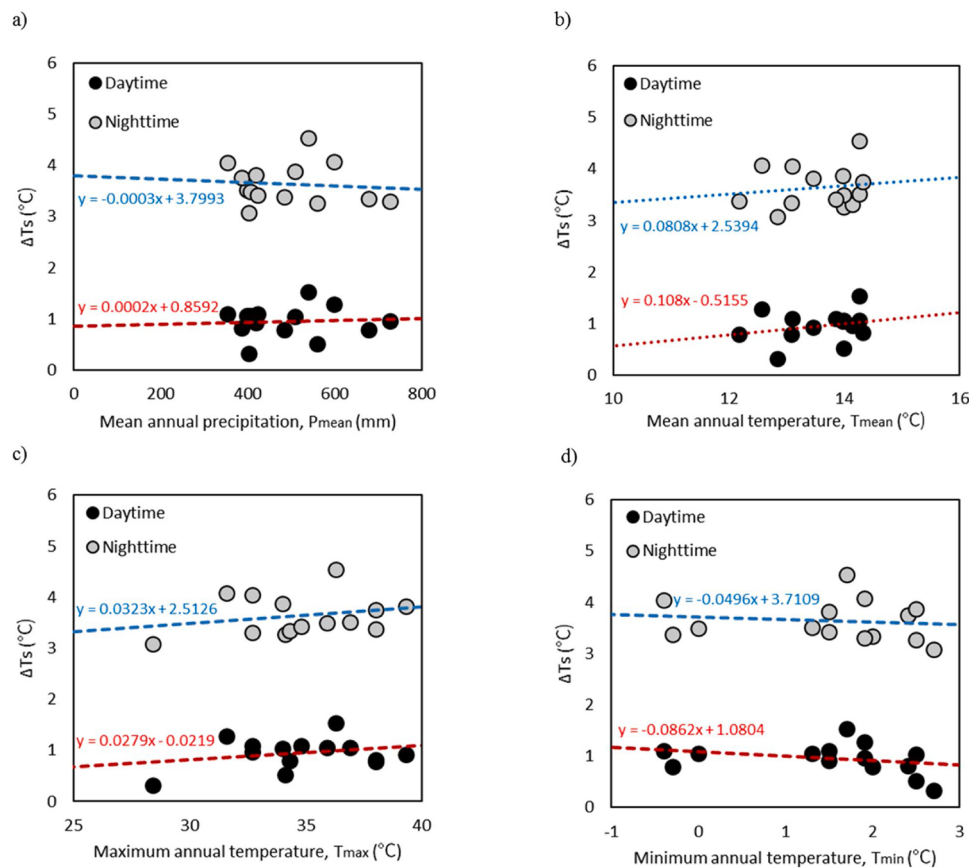


Fig. 7. Relationship of simulated daytime and nighttime ΔT with a) mean annual precipitation, b) mean annual temperature, c) maximum annual temperature, and d) minimum annual temperature in Melbourne from 2001 to 2014.

Meanwhile, the positive phase of IOD is more prominent to the extreme T_{max} compared to the negative IOD phase. On the other hand, the positive correlation between ΔT and T_{mean} revealed that ΔT was higher in warmer climate conditions (Zhou et al., 2016). Overall, the results indicated that ΔT was associated with P_{mean} , T_{mean} , and T_{max} and, consequently, showed correlation with SAM, ENSO, and IOD in Melbourne. Previous climate study in Australia also suggested that the hydroclimatic variability were largely related to the three climate modes which are SAM, ENSO, and IOD (King, Klingaman et al., 2014)

3.3. UHI component attributions under different hydroclimatic events

To further investigate the attributes of the components for UHI intensity, analysis based on the surface energy balance equation was performed over the study period (Eq. (5)). Individual components of radiation balance (Term 1), convection efficiency (Term 2), surface evaporative cooling (Term 3), heat storage (Term 4), and anthropogenic heat (Term 5) were obtained for daytime and nighttime. We also compared the UHI intensity from biophysical analysis with the CLM simulation (A_{CLM}). In this study, we used more than one indicator to describe UHI intensity for a more justifiable and reliable UHI definition, as suggested by Schwarz et al. (2011).

Fig. 8 shows the different trends of UHI component attributions during multiple hydro climatic events ('big dry', 'big wet', and 'angry summer'), and also during the 'transition' and 'average' period in Melbourne. The 'big dry' period from 2001 to 2009 showed the highest UHI intensity from biophysical attributions for both daytime and nighttime with 2.33 °C and 4.39 °C, respectively (Table 5). This occurrence was observed due to the 'big dry' that appears to be linked with high temperature in Melbourne which consequently increases the UHI intensity (Ummenhofer et al., 2009). The similar trend was also indicated from

CLM with ΔT of 1.29 °C during daytime and 4.08 °C during nighttime. Meanwhile, inconsistent UHI trend were demonstrated during 'big wet', 'transition', and 'angry summer' period for both daytime and nighttime.

During the 'big dry' event, evaporative cooling was the major factor for daytime UHI with 2.37 °C intensity related to Term 3 (Table 5). 'Big dry' or also known as 'Millennium drought' has ended with one of the worst bushfires occurred in southeastern part of Australia in late 2009 (Reeder et al., 2015). The UHI during 'big dry' that was strongly influenced by the evaporation cooling might due to the domestic water restrictions in Melbourne from several years of drought event (Nicholls, 2004). Besides, low precipitation and water availability during this period also contributed to the significant role of vegetation fraction for water storage during evaporation, which lead to higher water retention in vegetation compared to the urban area (Fitria et al., 2019).

However, during 'big wet' event, the convection efficiency was more major factor with 0.97 °C (2.13 °C) contribution towards daytime (nighttime) UHI associated with aerodynamic roughness in Term 2. Higher precipitation and cloud cover fraction during 'big wet' has led to the major contribution of convection process towards UHI intensity. Convection is less efficient to dissipate heat from urban land compared to rural land during this period, which contributed to the dominance of the overall ΔT during this period (Zhao et al., 2014). In addition, UHI attributions for 'average' period that covers total study period from 2001 to 2014 also experienced less efficient convection for daytime and nighttime UHI. This variability might due to the aerodynamic resistance estimated by Q_h which indicated that the selected rural site was characterized by highly dense vegetation and was aerodynamically rough (Zhao et al., 2014).

In contrast, the UHI intensity were highly influenced by heat storage during the 'angry summer' event, related to Term 4. Heat storage had greater impact of UHI because the exceptionally dry conditions during

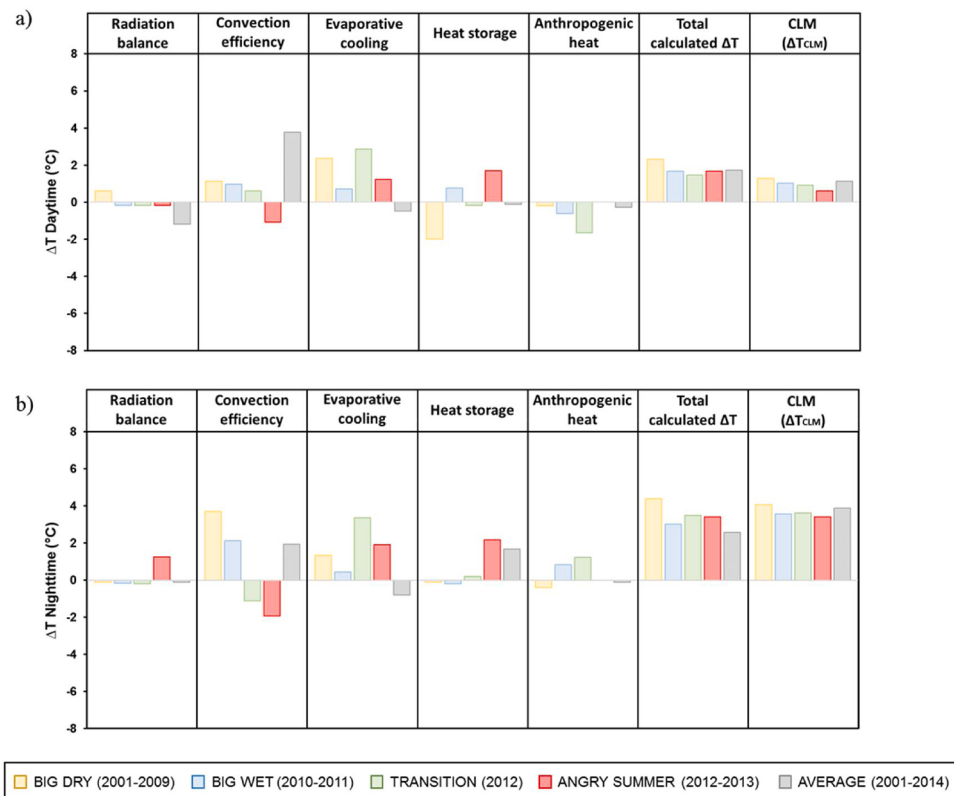


Fig. 8. UHI estimation during the a) daytime and b) nighttime based on component attributes analysis of radiation balance (Term 1), convection efficiency (Term 2), evaporative cooling (Term 3), heat storage (Term 4), and anthropogenic heat (Term 5) with total calculated ΔT and simulated ΔT from CLM (ΔT_{CLM}) during 'big dry', 'big wet', 'transition', 'angry summer', and 'average' periods at the Melbourne city. Term 1 to Term 5 represent total UHI contributions from Eq. (5).

this period has led to the extreme heat conditions over the eastern part of Australia (King, Karoly et al., 2014). Table 5 showed that the heat storage release had greater impact at nighttime compared to daytime with 2.16°C and 1.69°C , respectively. Additionally, the dominant contributor of heat storage during the night was observed due to the higher amount of heat stored in the impervious surface during the daytime (Fitria et al., 2019).

Overall, daytime and nighttime ΔT_{CLM} showed a similar pattern to the total calculated ΔT . 'Big dry' and 'angry summer' that indicated drought season in Melbourne showed major contribution of UHI towards evaporative cooling and heat storage, related to Term 3 and Term 4 respectively. Meanwhile, convection efficiency (Term 2) is more influential driver during 'big wet' with the abundance precipitation occurrence from 2010 to 2011. The average UHI for total period of 14 years also indicated major contribution towards convection efficiency which might due to the high vegetation in the rural site and the water resources availability. Furthermore, although the total study period includes multiple hydroclimatic events in Melbourne, water availability was able to quickly replenish after drought events and very slowly diminished after the wet events (Xie et al., 2019).

3.3.1. Quantification of UHI linked LULC and climate change

The LULC change altered the physical characteristics of the land surface, which consequently affected the background climate change and could inevitably act as feedback or a response toward climate variations (Findell et al., 2017; Foley et al., 2005; van der Molen et al., 2011). The highest urbanization rate concentrated on a specific area was

prone to SAM variations that were dominant in the coastal part of southeastern Australia. For this analysis, we distinguished the effects of background climate for daytime and nighttime ΔT based on UHI component attribute analysis with P_{mean} , T_{mean} , T_{max} , and T_{min} from 2001 to 2014, as shown in Fig. 9 and Table 6.

From this analysis, radiation balance (Term 1) indicated a negative UHI trend as precipitation increased during the daytime with correlation coefficient, R value of -0.14 (Fig. 9a). This trend occurred due to negative urban albedo differences that contributed to a reduction in UHI intensity, which indicated higher albedo in urban areas than rural surroundings, consistent with Manoli et al. (2019). Convection efficiency (Term 2) also indicated negative UHI trends ($R = -0.24$) with increasing precipitation, where higher precipitation decreased the energy redistribution factors in Term 2. Conversely, higher daytime and nighttime heat storage (Term 4) increased P_{mean} , while radiation balance increased P_{mean} during the nighttime, with R values of 0.06, 0.02, and 0.20, respectively.

Regarding the effects of UHI component attributes on T_{mean} , T_{max} , and T_{min} , the relationships were primarily controlled by convection efficiency, which was related to Term 2. Our analysis suggests that convection reduction had a notable positive dependence on T_{mean} , T_{max} , and T_{min} during the daytime ΔT (Fig. 9b-d) with R values of 0.22, 0.34, and 0.09 respectively, while increasing convection efficiency for nighttime ΔT showed a positive correlation with T_{mean} and T_{min} indicated by R values of 0.29 and 0.22 (Fig. 9f, h).

Meanwhile, surface evaporative cooling (Term 3) showed major contributions from UHI with T_{mean} and T_{max} for nighttime ΔT , with

Table 5
Biophysical contributions to UHI at daytime and nighttime based on component attributes analysis of radiation balance (Term 1), convection efficiency (Term 2), evaporative cooling (Term 3), heat storage (Term 4), and anthropogenic heat (Term 5) with total calculated ΔT and simulated ΔT from CLM (ΔT_{CLM}) during ‘big dry’, ‘big wet’, ‘transition’, ‘angry summer’, and ‘average’ periods at the Melbourne city. All units in $^{\circ}\text{C}$.

	Daytime			Nighttime			CLM (ΔT_{CLM})	Total calculated ΔT	ΔT CLM (ΔT_{CLM})
	Radiation balance	Convection efficiency	Evaporative cooling	Heat storage	Anthropogenic heat	Total calculated ΔT			
Big dry (2001–2009)	0.62	1.12	2.37	-1.97	0.20	2.33	1.29	-0.12	3.71
Big wet (2010–2011)	-0.16	0.97	0.72	0.76	-0.62	1.67	1.01	-0.18	2.13
Transition (2012)	-0.18	0.61	2.85	-0.17	-1.64	1.47	0.92	-0.19	1.12
Angry summer (2012–2013)	-0.17	-1.09	1.23	1.69	0.00	1.66	0.60	1.25	-1.94
Average (2001–2014)	-1.19	3.77	-0.47	-0.13	-0.26	1.73	1.12	-0.11	1.93
							-0.79	1.66	-0.13
								2.57	3.88

correlation coefficient of 0.06 and 0.44, respectively (Fig. 9f, g). This outcome suggests that a higher Bowen ratio estimated from Q_h and Q_e would increase T_{mean} and T_{max} as nighttime urban warming increased, which was associated with Term 3. The results of previous studies conducted at North American sites at similar latitudes also found that higher Bowen ratio values were dominant to drier and warmer climates across the urban surfaces (Grimmond & Oke, 1995). In addition, heat storage release also affected T_{max} during the daytime ΔT with $R = 0.21$, which was related to Term 4 (Fig. 9c). Land alterations toward urbanization decreased absorption of net shortwave radiation, which was dependent on heat storage release, as a part of climate patterns (Lee et al., 2011). This conversion also led to stronger convection and convergence and, therefore, altered the patterns of land-sea breezes and local thermodynamic conditions (Wang et al., 2014).

Overall, the results from this analysis showed that each UHI component’s attributes played a different key role in affecting local climate variations based on precipitation and temperature variations across Melbourne. Radiation balance, convection efficiency, evaporative cooling, heat storage release and anthropogenic heat were major contributors of UHI components that affected both precipitation and temperature variations and were correlated with both LULC and climate change for daytime and nighttime ΔT .

4. Conclusion

This study assessed UHI intensity and its relationships with LULC and climate change variations in Melbourne, Australia, by integrating the CLM simulation approach. In general, CLM version 4 showed adequate performance in simulating UHI intensity and temporal trends of ΔT for 14-years, from 2001 to 2014. The conversion of vegetated land into urban land increased impervious surface roughness and T_s in the urban area. Urban and built-up area also significantly contributed to the UHI effect with positive values of LCI, while grasslands had the lowest contribution effect. The LULC alteration also led to higher Q_h and significantly lower Q_e with a consequently higher ΔT intensity in the year 2014. Besides, simulated ΔT correlated with climate parameters due to the higher heat stored in soil moisture explained by precipitation events (P_{mean}), a strong relationship between UHI warming and SAM that influenced T_{max} and warmer background climate conditions (T_{mean}). For the component attributions of UHI, the individual factors corresponded differently during multiple hydroclimatic extreme events in the study area. This outcome proved that, besides the land use changes, UHI and its attributions component also linked with climate variations in Melbourne, Australia.

Overall, our results showed the interactions among UHI, LULC and climate variations in Melbourne, Australia. Our findings could be incorporated with the understanding of climate mitigation and the urbanization of the metropolitan city of Melbourne. However, some limitations might be addressed in this study and several works need to be further explored. The available urban flux tower with the urban landscape of open mid-rise (LCZ_6) might underestimate the UHI effect in this study. Other than that, this study particularly focused on the interactions between UHI with LULC and climate variations in the coastal city of Australia namely Melbourne, which is prone to the Southern Annular Mode (SAM) event. Hence, future studies can be conducted considering various cities in Australia to explore the relationship between UHI, LULC and their climate projections. Additionally, the contribution of land changes towards UHI in this study were quantified based on the land composition analysis, we will consider other land use type indices such as the land configuration metrics in our future works to validate the total effect of land use type towards UHI, along with their shape complexity and variability. Besides, the simulation of dynamic land use represented by CLM or other land model components are also recommended for future studies.

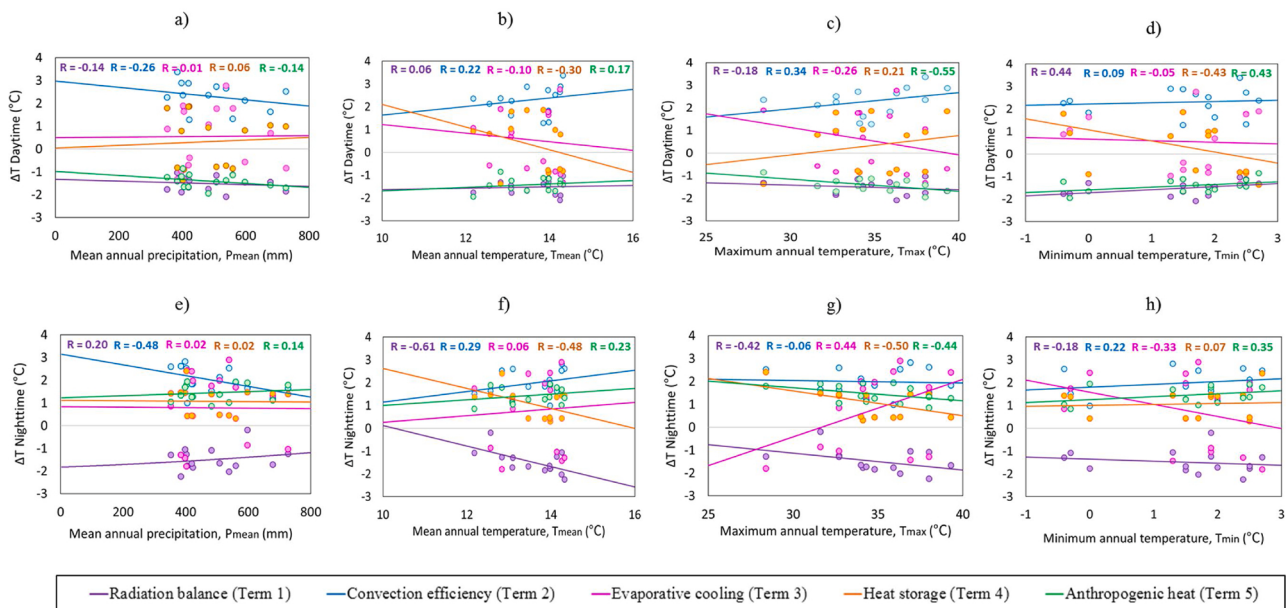


Fig. 9. Effects of daytime and nighttime UHI component attributes on radiation balance (Term 1), convection efficiency (Term 2), evaporative cooling (Term 3), heat storage (Term 4), and anthropogenic heat (Term 5) on background climate for mean annual precipitation (a, e), mean annual temperature (b, f), maximum annual temperature (c, g), and minimum annual temperature (d, h).

Table 6

Coefficient correlations between each component of UHI biophysical mechanism and the climate variables of mean annual precipitation (P_{mean}), mean annual temperature (T_{mean}), maximum annual temperature (T_{max}), and minimum annual temperature (T_{min}).

	Daytime				Nighttime			
	P_{mean}	T_{mean}	T_{max}	T_{min}	P_{mean}	T_{mean}	T_{max}	T_{min}
Radiation balance	-0.14	0.06	-0.18	0.44	0.20	-0.61	-0.42	-0.18
Convection efficiency	-0.26	0.22	0.34	0.09	-0.48	0.29	-0.06	0.22
Evaporative cooling	0.01	-0.10	-0.26	-0.05	0.02	0.06	0.44	-0.33
Heat storage	0.06	-0.30	0.21	-0.43	0.02	-0.48	-0.50	0.07
Anthropogenic heat	-0.14	0.17	-0.55	0.43	0.14	0.23	-0.44	0.35

Declaration of Competing Interest

The authors declare that they have no known competing financial interests or personal relationships that could have appeared to influence the work reported in this paper.

Acknowledgements

This work was supported by the National Research Foundation of Korea (NRF) grant funded by the Korea government (MSIT) (NRF-2019R1A2B5B01070196). We would like to thank the Urban-PLUMBER Project and Monash University, Australia for kindly providing the flux tower data at urban Preston site. This work also used eddy covariance data acquired and shared by the FLUXNET community, including these networks: AmeriFlux, AfriFlux, AsiaFlux, CarboAfrica, CarboEuropeIP, CarboItaly, CarboMont, ChinaFlux, Fluxnet-Canada, GreenGrass, ICOS, KoFlux, LBA, NECC, OzFlux-TERN, TCOS-Siberia, and USCCC. The ERA-Interim reanalysis data are provided by ECMWF and processed by LSCE. The FLUXNET eddy covariance data processing and harmonization was carried out by the European Fluxes Database Cluster, AmeriFlux Management Project, and Fluxdata project of FLUXNET, with the support of CDIAC and ICOS Ecosystem Thematic Center, and the OzFlux, ChinaFlux and AsiaFlux offices. We would like to thank the OzFlux (especially AU-Wom site) to provide the flux data from the FLUXNET2015 Dataset website freely (<http://fluxnet.fluxdata.org/data/fluxnet2015-dataset/>). We acknowledge the National Aeronautics and Space Administration (NASA) for providing the Moderate Resolution Imaging Spectroradiometer (MODIS) Land Cover Type (MCD12Q1) and Land Surface

Temperature (MYD11A2).

References

- Adams, M. P., & Smith, P. L. (2014). A systematic approach to model the influence of the type and density of vegetation cover on urban heat using remote sensing. *Landscape and Urban Planning*, 132(August 2003), 47–54. <https://doi.org/10.1016/j.landurbplan.2014.08.008>
- Amin, I. M. Z., bin, M., Ercan, A., Ishida, K., Kavvas, M. L., Chen, Z. Q., & Jang, S. H. (2019). Impacts of climate change on the hydro-climate of peninsular Malaysia. *Water (Switzerland)*, 11(9). <https://doi.org/10.3390/w11091798>
- Betts, R. A., Falloon, P. D., Goldeijk, K. K., & Ramankutty, N. (2007). Biogeophysical effects of land use on climate: Model simulations of radiative forcing and large-scale temperature change. *Agricultural and Forest Meteorology*, 142(2–4), 216–233. <https://doi.org/10.1016/j.agrformet.2006.08.021>
- Brook, T. (2015). Temperature and precipitation extremes. *The troubled empire*. <https://doi.org/10.4159/9780674056206-012>
- Bureau of Meteorology. (2013). *Special Climate Statement 43 – extreme heat in January 2013*. February (pp. 1–19) <http://www.bom.gov.au/climate/current/statements/scs43e.pdf>.
- Cao, C., Lee, X., Liu, S., Schultz, N., Xiao, W., Zhang, M., & Zhao, L. (2016). Urban heat islands in China enhanced by haze pollution. *Nature Communications*, 7, 1–7. <https://doi.org/10.1038/ncomms12509>
- Chapman, S., Watson, J. E. M., Salazar, A., Thatcher, M., & McAlpine, C. A. (2017). The impact of urbanization and climate change on urban temperatures: A systematic review. *Landscape Ecology*, 32(10), 1921–1935. <https://doi.org/10.1007/s10980-017-0561-4>
- Chen, S., Li, W. B., Du, Y. D., Mao, C. Y., & Zhang, L. (2015). Urbanization effect on precipitation over the Pearl River Delta based on CMORPH data. *Advances in Climate Change Research*, 6(1), 16–22. <https://doi.org/10.1016/j.accre.2015.08.002>
- Chung, Y. S., Yoon, M. B., & Kim, H. S. (2004). On climate variations and changes observed in South Korea. *Climatic Change*, 66(1–2), 151–161. <https://doi.org/10.1023/B:CLIM.0000043141.54763.f8>

- Coutts, A. M., Beringer, J., & Tapper, N. J. (2007a). Characteristics influencing the variability of urban CO₂ fluxes in Melbourne, Australia. *Atmospheric Environment*, *41* (1), 51–62. <https://doi.org/10.1016/j.atmosenv.2006.08.030>
- Coutts, A. M., Beringer, J., & Tapper, N. J. (2007b). Impact of increasing urban density on local climate: Spatial and temporal variations in the surface energy balance in Melbourne, Australia. *Journal of Applied Meteorology and Climatology*, *46*(4), 477–493. <https://doi.org/10.1175/JAM2462.1>
- Daramola, M. T., & Balogun, I. A. (2019). Local climate zone classification of surface energy flux distribution within an urban area of a hot-humid tropical city. *Urban Climate*, *29*(July), 100504. <https://doi.org/10.1016/j.ulclim.2019.100504>
- Dirmeyer, P. A., Chen, L., Wu, J., Shin, C. S., Huang, B., Cash, B. A., Bosilovich, M. G., Mahanama, S., Koster, R. D., Santanello, J. A., Ek, M. B., Balsamo, G., Dutra, E., & Lawrence, D. M. (2018). Verification of land-atmosphere coupling in forecast models, reanalyses, and land surface models using flux site observations. *Journal of Hydrometeorology*, *19*(2), 375–392. <https://doi.org/10.1175/JHM-D-17-0152.1>
- Findell, K. L., Berg, A., Gentile, P., Krasting, J. P., Lintner, B. R., Malyshov, S., Santanello, J. A., & Sheviakova, E. (2017). The impact of anthropogenic land use and land cover change on regional climate extremes. *Nature Communications*, *8*(1), 1–9. <https://doi.org/10.1038/s41467-017-01038-w>
- Fitrria, R., Kim, D., Baik, J., & Choi, M. (2019). Impact of biophysical mechanisms on urban heat island associated with climate variation and urban morphology. *Scientific Reports*, *9*(1), 1–13. <https://doi.org/10.1038/s41598-019-55847-8>
- Foley, J. A., DeFries, R., Asner, G. P., Barford, C., Bonan, G., Carpenter, S. R., Chapin, F. S., Coe, M. T., Daily, G. C., Gibbs, H. K., Helkowski, J. H., Holloway, T., Howard, E. A., Kucharik, C. J., Monfreda, C., Patz, J. A., Prentice, I. C., Ramankutty, N., & Snyder, P. K. (2005). Global consequences of land use. *Science*, *309*(5734), 570–574. <https://doi.org/10.1126/science.1111772>
- Gao, M., Shen, H., Han, X., Li, H., & Zhang, L. (2018). Multiple timescale analysis of the urban heat island effect based on the Community Land Model: a case study of the city of Xi'an, China. *Environmental Monitoring and Assessment*, *190*(1). <https://doi.org/10.1007/s10661-017-6320-9>
- Grimmond, C. S. B., & Oke, T. R. (1995). *Comparison of heat fluxes from summertime observations in the suburbs of four North American cities* (Vol. 93).
- Hart, M. A., & Sailor, D. J. (2009). Quantifying the influence of land-use and surface characteristics on spatial variability in the urban heat island. *Theoretical and Applied Climatology*, *95*(3–4), 397–406. <https://doi.org/10.1007/s00704-008-0017-5>
- Heberger, M. (2019). *Australia's millennium drought: Impacts and responses*. June. <https://doi.org/10.5822/978-1-59726-228-6>.
- Hendon, H. H., Thompson, D. W. J., & Wheeler, M. C. (2007). Australian rainfall and surface temperature variations associated with the Southern Hemisphere annular mode. *Journal of Climate*, *20*(11), 2452–2467. <https://doi.org/10.1175/JCLI4134.1>
- Huang, Q., Huang, J., Yang, X., Fang, C., & Liang, Y. (2019). Quantifying the seasonal contribution of coupling urban land use types on Urban Heat Island using Land Contribution Index: A case study in Wuhan, China. *Sustainable Cities and Society*, *44* (September 2018), 666–675. <https://doi.org/10.1016/j.scs.2018.10.016>
- Imran, H. M., Kala, J., Ng, A. W. M., & Muthukumaran, S. (2019). Effectiveness of vegetated patches as Green Infrastructure in mitigating Urban Heat Island effects during a heatwave event in the city of Melbourne. *Weather and Climate Extremes*, *25* (June). <https://doi.org/10.1016/j.wace.2019.100217>
- Jackson, T. L., Feddema, J. J., Oleson, K. W., Bonan, G. B., & Bauer, J. T. (2010). Parameterization of urban characteristics for global climate modeling. *Annals of the Association of American Geographers*, *100*(4), 848–865. <https://doi.org/10.1080/00045608.2010.497328>
- Jakob, D., & Walland, D. (2016). Variability and long-term change in Australian temperature and precipitation extremes. *Weather and Climate Extremes*, *14*, 36–55. <https://doi.org/10.1016/j.wace.2016.11.001>
- Jamei, Y., Rajagopalan, P., & Sun, Q. C. (2019). Spatial structure of surface urban heat island and its relationship with vegetation and built-up areas in Melbourne, Australia. *The Science of the Total Environment*, *659*, 1335–1351. <https://doi.org/10.1016/j.scitotenv.2018.12.308>
- Kawamura, A., McKerchar, A. I., Spigel, R. H., & Jinno, K. (1998). Chaotic characteristics of the Southern Oscillation Index time series. *Journal of Hydrology*, *204*(1–4), 168–181. [https://doi.org/10.1016/S0022-1694\(97\)00129-7](https://doi.org/10.1016/S0022-1694(97)00129-7)
- Keay, K., & Simmonds, I. (2005). The association of rainfall and other weather variables with road traffic volume in Melbourne, Australia. *Accident Analysis and Prevention*, *37* (1), 109–124. <https://doi.org/10.1016/j.aap.2004.07.005>
- Kiehl, J. T., & Gent, P. R. (2004). The community climate system model, version 2. *Journal of Climate*, *17*(19), 3666–3682. [https://doi.org/10.1175/1520-0442\(2004\)017<3666:TCCSMV>2.0.CO;2](https://doi.org/10.1175/1520-0442(2004)017<3666:TCCSMV>2.0.CO;2)
- Kim, D., Lim, Y. J., Kang, M., & Choi, M. (2016). Land response to atmosphere at different resolutions in the common land model over East Asia. *Advances in Atmospheric Sciences*, *33*(3), 391–408. <https://doi.org/10.1007/s00376-015-5059-x>
- King, A. D., Lewis, S. C., Perkins, S. E., Alexander, L. V., Donat, M. G., Karoly, D. J., & Black, M. T. (2013). Limited evidence of anthropogenic influence on the 2011–12 Extreme Rainfall over Southeast Australia. *Bulletin of the American Meteorological Society*, *94*(9), S55–S58.
- King, A. D., Karoly, D. J., Donat, M. G., & Alexander, L. (2014). Climate change turns Australia's 2013 big dry into a year of record-breaking heat. *Bulletin of the American Meteorological Society*, *95*(9), S41–S45.
- King, A. D., Klingaman, N. P., Alexander, L. V., Donat, M. G., Jourdain, N. C., & Maher, P. (2014). Extreme rainfall variability in Australia: Patterns, drivers, and predictability. *Journal of Climate*, *27*(15), 6035–6050. <https://doi.org/10.1175/JCLI-D-13-00715.1>
- Lawrence, D. M., Oleson, K. W., Flanner, M. G., Thornton, P. E., Swenson, S. C., Lawrence, P. J., Zeng, X., Yang, Z.-L., Levis, S., Sakaguchi, K., Bonan, G. B., & Slater, A. G. (2011). Parameterization improvements and functional and structural advances in version 4 of the Community Land Model. *Journal of Advances in Modeling Earth Systems*, *3*(3), 1–27. <https://doi.org/10.1029/2011ms00045>
- Lee, X., Goulden, M. L., Hollinger, D. Y., Barr, A., Black, T. A., Bohrer, G., Bracho, R., Drake, B., Goldstein, A., Gu, L., Katul, G., Kolb, T., Law, B. E., Margolis, H., Meyers, T., Monson, R., Munger, W., Oren, R., Tha Paw U, K., ... Zhao, L. (2011). Observed increase in local cooling effect of deforestation at higher latitudes. *Nature*, *479*(7373), 384–387. <https://doi.org/10.1038/nature10588>
- Li, D., Sun, T., Liu, M., Yang, L., Wang, L., & Gao, Z. (2015). Contrasting responses of urban and rural surface energy budgets to heat waves explain synergies between urban heat islands and heat waves. *Environmental Research Letters*, *10*(5). <https://doi.org/10.1088/1748-9326/10/5/054009>
- Li, J., Song, C., Cao, L., Zhu, F., Meng, X., & Wu, J. (2011). Impacts of landscape structure on surface urban heat islands: A case study of Shanghai, China. *Remote Sensing of Environment*, *115*(12), 3249–3263. <https://doi.org/10.1016/j.rse.2011.07.008>
- Ma, E., Deng, X., Zhang, Q., & Liu, A. (2014). Spatial variation of surface energy fluxes due to land use changes across China. *Energies*, *7*(4), 2194–2206. <https://doi.org/10.3390/en7042194>
- Manoli, G., Fatichi, S., Schläpfer, M., Yu, K., Crowther, T. W., Meili, N., Burlando, P., Katul, G. G., & Bou-Zeid, E. (2019). Magnitude of urban heat islands largely explained by climate and population. *Nature*, *573*(7772), 55–60. <https://doi.org/10.1038/s41586-019-1512-9>
- Marshall, A. G., Hemer, M. A., Hendon, H. H., & McInnes, K. L. (2018). Southern annular mode impacts on global ocean surface waves. *Ocean Modelling*, *129*(July), 58–74. <https://doi.org/10.1016/j.ocemod.2018.07.007>
- Menezes, V. V., & Vianna, M. L. (2019). Quasi-biennial Rossby and Kelvin waves in the South Indian Ocean: Tropical and subtropical modes and the Indian ocean dipole. *Deep-Sea Research Part II: Topical Studies in Oceanography*, *166*(April), 43–63. <https://doi.org/10.1016/j.dsr.2019.05.002>
- Morris, C. J. G., & Simmonds, I. (2001). Quantification of the influence of wind and cloud on the nocturnal urban heat island of a large city. *Journal of Applied Meteorology*, *40* (2), 169–182. [https://doi.org/10.1175/1520-0450\(2001\)040<0169:QOTIOW>2.0.CO;2](https://doi.org/10.1175/1520-0450(2001)040<0169:QOTIOW>2.0.CO;2)
- Murphy, F. B., & Timbal, B. (2008). A review of recent climate variability and climate change in southeastern Australia. *International Journal of Climatology*, *29*(March 2008), 2011–2029. <https://doi.org/10.1002/joc>
- Nicholls, N. (2004). The changing nature of Australian droughts. *Climatic Change*, *63*(3), 323–336. <https://doi.org/10.1023/B:CLIM.0000018515.46344.6d>
- Ogden, F. L., Allen, M. B., Lai, W., Zhu, J., Seo, M., Douglas, C. C., & Talbot, C. A. (2015). The integrated urban land model. *Journal of Advances in Modeling Earth Systems*, *7*, 1339–1350. <https://doi.org/10.1002/2017MS001065>
- Oke, T. R. (1988). The urban energy balance. *Progress in Physical Geography*, *12*(4), 471–508. <https://doi.org/10.1177/03091338801200401>
- Oke, T. R., Johnson, G. T., Steyn, D. G., & Watson, I. D. (1991). Simulation of surface urban heat islands under "ideal" conditions at night part 2: Diagnosis of causation. *Boundary-Layer Meteorology*, *56*(4), 339–358. <https://doi.org/10.1007/BF00119211>
- Oleson, K. W., & Bonan, G. (2010). *Technical description of an urban parameterization for the Community Land Model (CLMU)*. Tech. Note NCAR. April <http://nldr.library.ucar.edu/repository/assets/technotes/asset-000-000-000-848.pdf>
- Oleson, K. W., Lawrence, D. M., Bonan, G. B., Drewniak, B., Huang, M., Koven, C. D., Levis, S., Li, F., Riley, W. J., Subin, Z. M., Swenson, S. C., Thornton, P. E., Bozbayik, A., Fisher, R., Heald, C. L., Kluzek, E., Lamarque, J.-F., Lawrence, P. J., Leung, L. R., ... Yang, Z.-L. (2013). *Technical description of version 4.5 of the Community Land Model (CLM)*. April, NCAR/TN-503+STR. http://www.cesm.ucar.edu/models/clsm1.2/clm/CLM45_Tech_Note.pdf
- Pastorello, G., Trottia, C., Canfora, E., Chu, H., Christianson, D., Cheah, Y. W., Poindexter, C., Chen, J., Elbashandy, A., Humphrey, M., Isaac, P., Polidori, D., Ribeca, A., van Ingen, C., Zhang, L., Amiro, B., Ammann, C., Arain, M. A., Ardö, J., ... Papale, D. (2020). The FLUXNET2015 dataset and the ONEFlux processing pipeline for eddy covariance data. *Scientific Data*, *7*(1), 225. <https://doi.org/10.1038/s41597-020-0534-3>
- Peng, S., Piao, S., Ciais, P., Friedlingstein, P., Ottle, C., Bréon, F. M., Nan, H., Zhou, L., & Myneni, R. B. (2012). Surface urban heat island across 419 global big cities. *Environmental Science & Technology*, *46*(2), 696–703. <https://doi.org/10.1021/es2030438>
- Phelan, P. E., Kaloush, K., Miner, M., Golden, J., Phelan, B., Silva, H., & Taylor, R. A. (2015). Urban Heat Island: Mechanisms, implications, and possible remedies. *Annual Review of Environment and Resources*, *40*(1), 285–307. <https://doi.org/10.1146/annurev-environ-102014-021155>
- Rayner, N. A., Parker, D. E., Horton, E. B., Folland, C. K., Alexander, L. V., Rowell, D. P., Kent, E. C., & Kaplan, A. (2003). Global analyses of sea surface temperature, sea ice, and night marine air temperature since the late nineteenth century. *Journal of Geophysical Research Atmospheres*, *108*(14). <https://doi.org/10.1029/2002jd002670>
- Reeder, M. J., Spengler, T., & Musgrave, R. (2015). Rossby waves, extreme fronts, and wildfires in southeastern Australia. *Geophysical Research Letters*, *42*(6), 2015–2023. <https://doi.org/10.1002/2015GL063125>
- Rizwan, A. M., Dennis, L. Y. C., & Liu, C. (2008). A review on the generation, determination and mitigation of Urban Heat Island. *Journal of the Environmental Sciences*, *20*(1), 120–128. [https://doi.org/10.1016/S1001-0742\(08\)60019-4](https://doi.org/10.1016/S1001-0742(08)60019-4)
- Rodell, M., Houser, P. R., Jambor, U., Gottschalck, J., Mitchell, K., Meng, C. J., Arseneault, K., Cosgrove, B., Radakovitch, J., Bosilovich, M., Entin, J. K., Walker, J. P., Lohmann, D., & Toll, D. (2004). The global land data assimilation system. *Bulletin of the American Meteorological Society*, *85*(3), 381–394. <https://doi.org/10.1175/BAMS-85-3-381>
- Saji, N. H., Goswami, B. N., Vinayachandran, P. N., & Yamagata, T. (1999). A dipole mode in the tropical Indian ocean. *Nature*, *401*(6751), 360–363. <https://doi.org/10.1038/43854>

- Salimi, M., & Al-Ghamdi, S. G. (2020). Climate change impacts on critical urban infrastructure and urban resiliency strategies for the Middle East. *Sustainable Cities and Society*, 54, Article 101948. <https://doi.org/10.1016/j.scs.2019.101948>
- Salleh, S. A., Latif, Z. A., Chan, A., Morris, K. I., Ooi, M. C. G., & Mohd, W. M. N. W. (2015). Weather Research Forecast (WRF) modification of land surface albedo simulations for urban near surface temperature. *International Conference on space science and communication, icons pace, 2015-Septe*, 243–247. <https://doi.org/10.1109/Icospace.2015.7283787>
- Schwarz, N., Lautenbach, S., & Seppelt, R. (2011). Exploring indicators for quantifying surface urban heat islands of European cities with MODIS land surface temperatures. *Remote Sensing of Environment*, 115(12), 3175–3186. <https://doi.org/10.1016/j.rse.2011.07.003>
- Serpetzoglou, E., Anagnostou, E. N., Papadopoulos, A., Nikolopoulos, E. I., & Maggioni, V. (2010). Error propagation of remote sensing rainfall estimates in soil moisture prediction from a land surface model. *Journal of Hydrometeorology*, 11(3), 705–720. <https://doi.org/10.1175/2009JHM1166.1>
- Sewell, T., Stephens, R. E., Dominey-Howes, D., Bruce, E., & Perkins-Kirkpatrick, S. (2016). Disaster declarations associated with bushfires, floods and storms in New South Wales, Australia between 2004 and 2014. *Scientific Reports*, 6(November), 1–11. <https://doi.org/10.1038/srep36369>
- Silva, J. S., da Silva, R. M., & Santos, C. A. G. (2018). Spatiotemporal impact of land use/land cover changes on urban heat islands: A case study of Paço do Lumiar, Brazil. *Building and Environment*, 136(March), 279–292. <https://doi.org/10.1016/j.buildenv.2018.03.041>
- Singh, P., Kikon, N., & Verma, P. (2017). Impact of land use change and urbanization on urban heat island in Lucknow city, Central India. A remote sensing based estimate. *Sustainable Cities and Society*, 32, 100–114. <https://doi.org/10.1016/j.scs.2017.02.018>
- Son, N. T., Chen, C. F., Chen, C. R., Thanh, B. X., & Vuong, T. H. (2017). Assessment of urbanization and urban heat islands in Ho Chi Minh City, Vietnam using Landsat data. *Sustainable Cities and Society*, 30, 150–161. <https://doi.org/10.1016/j.scs.2017.01.009>
- Stewart, I. D., & Oke, T. R. (2012). Local climate zones for urban temperature studies. *Bulletin of the American Meteorological Society*, 93(12), 1879–1900. <https://doi.org/10.1175/BAMS-D-11-00019.1>
- Stewart, I., & Oke, T. (2009). Classifying urban climate field sites by “local climate zones”: The case of Nagano, Japan. *The seventh international conference on urban climate, July*, 1–5.
- Sun, R., Lü, Y., Yang, X., & Chen, L. (2019). Understanding the variability of urban heat islands from local background climate and urbanization. *Journal of Cleaner Production*, 208, 743–752. <https://doi.org/10.1016/j.jclepro.2018.10.178>
- Taschetto, A. S., Sen Gupta, A., Ummenhofer, C. C., & England, M. H. (2016). Can Australian multiyear droughts and wet spells be generated in the absence of oceanic variability? *Journal of Climate*, 29(17), 6201–6221. <https://doi.org/10.1175/JCLI-D-15-0694.1>
- Torok, S. J., Morris, C. J. G., Skinner, C., & Plummer, N. (2001). Urban heat island features of southeast Australian towns. *Australian Meteorological Magazine*, 50(1), 1–13.
- Trenberth, K. E. (1984). Signal versus noise in the Southern Oscillation. *Monthly Weather Review*, 112, 326–332.
- Trenberth, K. E. (1997). The definition of El Niño. *Bulletin of the American Meteorological Society*, 78(12), 2771–2777. [https://doi.org/10.1175/1520-0477\(1997\)078<2771:TDOENO>2.0.CO;2](https://doi.org/10.1175/1520-0477(1997)078<2771:TDOENO>2.0.CO;2)
- Umair, M., Kim, D., & Choi, M. (2019). Impacts of land use/land cover on runoff and energy budgets in an East Asia ecosystem from remotely sensed data in a community land model. *The Science of the Total Environment*, 684, 641–656. <https://doi.org/10.1016/j.scitotenv.2019.05.244>
- Ummenhofer, C. C., England, M. H., McIntosh, P. C., Meyers, G. A., Pook, M. J., Risbey, J. S., Sen Gupta, A., & Taschetto, A. S. (2009). What causes southeast Australia's worst droughts? *Geophysical Research Letters*, 36(4), 1–5. <https://doi.org/10.1029/2008GL036801>
- Ummenhofer, C. C., Sen Gupta, A., Briggs, P. R., England, M. H., McIntosh, P. C., Meyers, G. A., Pook, M. J., Raupach, M. R., & Risbey, J. S. (2011). Indian and Pacific Ocean influences on southeast Australian drought and soil moisture. *Journal of Climate*, 24(5), 1313–1336. <https://doi.org/10.1175/2010JCLI3475.1>
- van der Molen, M. K., van den Hurk, B. J. J. M., & Hazeleger, W. (2011). A damped land use change climate response towards the tropics. *Climate Dynamics*, 37(9–10), 2035–2043. <https://doi.org/10.1007/s00382-011-1018-0>
- Van Dijk, A. I. J. M., Beck, H. E., Crosbie, R. S., De Jeu, R. A. M., Liu, Y. Y., Podger, G. M., Timbal, B., & Viney, N. R. (2013). The Millennium Drought in southeast Australia (2001–2009): Natural and human causes and implications for water resources, ecosystems, economy, and society. *Water Resources Research*, 49(2), 1040–1057. <https://doi.org/10.1002/wrcr.20123>
- van Lipzig, N. P. M., Marshall, G. J., Orr, A., & King, J. C. (2008). The relationship between the Southern Hemisphere annular mode and antarctic Peninsula summer temperatures: Analysis of a high-resolution model climatology. *Journal of Climate*, 21(8), 1649–1668. <https://doi.org/10.1175/2007JCLI1695.1>
- Wang, X., Liao, J., Zhang, J., Shen, C., Chen, W., Xia, B., & Wang, T. (2014). A numeric study of regional climate change induced by urban expansion in the Pearl River Delta, China. *Journal of Applied Meteorology and Climatology*, 53(2), 346–362. <https://doi.org/10.1175/JAMC-D-13-054.1>
- Winter, J. M., & Eltahir, E. A. B. (2010). The sensitivity of latent heat flux to changes in the radiative forcing: A framework for comparing models and observations. *Journal of Climate*, 23(9), 2345–2356. <https://doi.org/10.1175/2009JCLI3158.1>
- Wu, H., Ye, L. P., Shi, W. Z., & Clarke, K. C. (2014). Assessing the effects of land use spatial structure on urban heat islands using HJ-1B remote sensing imagery in Wuhan, China. *International Journal of Applied Earth Observation and Geoinformation*, 32(1), 67–78. <https://doi.org/10.1016/j.jag.2014.03.019>
- Xie, Z., Huete, A., Cleverly, J., Phinn, S., McDonald-Madden, E., Cao, Y., & Qin, F. (2019). Multi-climate mode interactions drive hydrological and vegetation responses to hydroclimatic extremes in Australia. *Remote Sensing of Environment*, 231(May), 111270. <https://doi.org/10.1016/j.rse.2019.111270>
- Yan, H., Sun, L., Wang, Y., Huang, W., Qiu, S., & Yang, C. (2011). A record of the Southern Oscillation Index for the past 2,000 years from precipitation proxies. *Nature Geoscience*, 4(9), 611–614. <https://doi.org/10.1038/ngeo1231>
- Yang, P., Ren, G., & Hou, W. (2019). Impact of daytime precipitation duration on urban heat island intensity over Beijing city. *Urban Climate*, 28(April), 100463. <https://doi.org/10.1016/j.uclim.2019.100463>
- Zhang, K., Wang, R., Shen, C., & Da, L. (2010). Temporal and spatial characteristics of the urban heat island during rapid urbanization in Shanghai, China. *Environmental Monitoring and Assessment*, 169(1–4), 101–112. <https://doi.org/10.1007/s10661-009-1154-8>
- Zhao, L., Lee, X., Smith, R. B., & Oleson, K. (2014). Strong contributions of local background climate to urban heat islands. *Nature*, 511(7508), 216–219. <https://doi.org/10.1038/nature13462>
- Zhou, B., Lauwaet, D., Hooyberghs, H., De Ridder, K., Kropp, J. P., & Rybski, D. (2016). Assessing seasonality in the surface urban heat island of London. *Journal of Applied Meteorology and Climatology*, 55(3), 493–505. <https://doi.org/10.1175/JAMC-D-15-0041.1>
- Zhou, B., Rybski, D., & Kropp, J. P. (2017). The role of city size and urban form in the surface urban heat island. *Scientific Reports*, 7(1), 1–9. <https://doi.org/10.1038/s41598-017-04242-2>
- Zhou, D., Zhao, S., Liu, S., Zhang, L., & Zhu, C. (2014). Surface urban heat island in China's 32 major cities: Spatial patterns and drivers. *Remote Sensing of Environment*, 152, 51–61. <https://doi.org/10.1016/j.rse.2014.05.017>